American Society of Mechanical Engineers

ASME Accepted Manuscript Repository

| Patrick Hubert Wagner | Wagner | mail@patrick-wagner.net |
| *First* | *Last* | *E-mail* |

ASME Paper Title: Modeling and Designing of a Radial Anode Off-Gas Recirculation Fan

for Solid Oxide Fuel Cell Systems

Authors: Patrick H. Wagner, Zacharie Wuillemin, Stefan Diethelm, Jan Van herle , Jürg Schiffmann

*VOR (version of record)

Patrick H. Wagner   1

Post-Print: Modelling and designing of a radial anode off-gas recirculation fan for Solid Oxide Fuel Cell systems

P. H. Wagner[a], Z. Wuillemin[b], S. Diethelm[ab], J. Van herle[a], J. Schiffmann[a]

[a] School of Engineering, École Polytechnique Fédérale de Lausanne, Lausanne 1015, Switzerland
[b] HTceramix, Yverdon-les-Bains 1400, Switzerland

To improve the industry benchmark of solid oxide fuel cell systems, we consider anode off-gas recirculation using a small-scale fan. Evolutionary algorithms compare different system design alternatives with hot or cold recirculation. The system performance is evaluated through multi-objective optimization criteria, i.e. maximization of electrical efficiency and cogeneration efficiency. The aerodynamic efficiency and rotordynamic stability of the high-speed recirculation fan is investigated in detail. The results obtained suggest that improvements to the best SOFC systems, in terms of net electrical efficiency, are achievable, including for small power scale (10 kW$_e$).

Introduction

Solid Oxide Fuel Cells (SOFC) were initially developed for high temperature operation (>900° C) [1]. The current state of the art SOFCs operate in an intermediate temperature range (600-800° C). They use a nickel yttria stabilized zirconia (Ni-YSZ) composite planar anode, a lanthanum strontium cobaltite ferrite (LSCF)/cerium gadolinium oxide (CGO) composite cathode, a thin YSZ/CGO double electrolyte, and FeCr metal interconnect plates/sheets as bulk materials.

The use of SOFCs for power generation is attractive, due to the high electrical efficiencies achievable even in the small-size power generation range [2]. Payne et al. [3] report 60% AC net electrical efficiency for the commercial 2 kW$_e$ BlueGen system. Nonetheless, there still exists a significant potential to even further improve the efficiency of integrated systems, which use natural gas or biogas processed through steam methane reforming, using external steam supply for stack integrated syngas production.

Anode off-gas recirculation (AOR) has been identified as a promising feature to further increase the SOFC system efficiency while reducing investment cost [4]. Since the recirculating feed contains steam produced in the stack, no more external steam supply is needed for reforming. This eliminates the use of expensive water de-ionization sets. Further, it allows for high overall fuel utilization at low diffusion losses, resulting in higher cell voltage, and improved SOFC efficiency [5]. The downside, however, is the additional complexity represented by the operation and control of the fan, which could lead to unstable stack operation. Nonetheless, several SOFC systems with AOR have already been demonstrated. Powell et al. [6] operated an SOFC with AOR from 1.65 to 2.15 kW$_e$ with 57% to 53% DC net electrical efficiency, while Halinen et al. [7,8] claim a 54% AC net electrical efficiency for a 10 kW$_e$ cross-flow SOFC with AOR.

The objective of this paper is an optimized 10 kW$_e$ SOFC system including the aerodynamic recirculator fan design for the AOR, the key novelty in this study. Note that all efficiencies in this paper are based on the lower heating value (LHV).

Methodology of optimization

The system flowsheet which includes models for balance of plant components, an experimentally validated SOFC stack model, and a 0D fan model based on similarity concepts, is solved by using the commercial software VALI by Belsim S.A. The design variables identified for this system are listed in Table I.

As shown in Figure 1 the design procedure implemented for this work is composed of two subtasks: (1) the Multi-Objective Optimization (MOO) of the SOFC system using a platform developed for the design and optimization of integrated energy systems called OSMOSE [9] and (2) the observation-based iterative fan modelling and designing.

The first subtask consists of four steps. Firstly, a process flowsheet with models of the individual components, including a sophisticated reduced order 0D fan model based on similarity concepts, is built. The flowsheet is solvable once the values of the previously mentioned design variables are specified. Secondly, using energy integration techniques, internal heat recovery within the system is maximized. Thereafter, performance of the system is evaluated with respect to the desired objectives. Lastly, an iterative optimization procedure is followed, using an evolutionary algorithm, where a physically bounded space of design variables is scanned. Successive generations of populations are obtained by reproduction and mutation of the existing population. Following the 'survival of the fittest' rule, the iteration is stopped when a non-dominated solution set represented by a Pareto-optimal front is obtained. A similar methodology was used by Facchinetti et al. [10] for the optimization of an SOFC combined with a small-scale gas turbine.

The second subtask consists of three steps. Based on the fan parameters from the optimization routine, a basic fan geometry is designed by calculating the velocity triangles on the mean line. The results are validated with a more detailed 3D Computational Fluid Dynamics (CFD) simulation using Ansys CFX. Finally, the rotordynamic stability of the gas-lubriacted bearing supported fan is investigated with an in-house Matlab code.
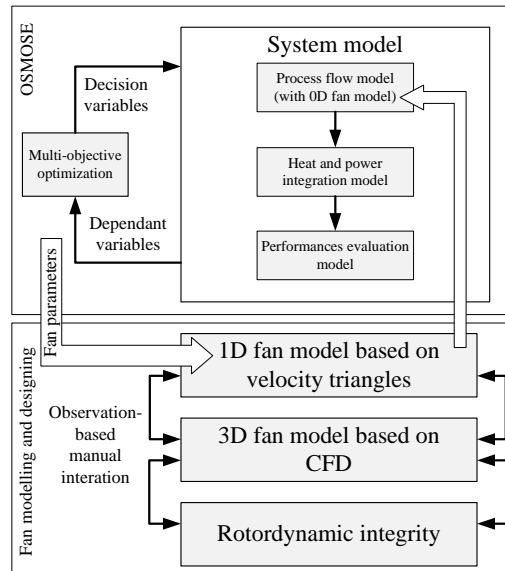

Figure 1. Methodology of the SOFC system optimization using OSMOSE and the fan modelling and designing

Table I. Decision variables and their range for the multi-objective optimization

Design variables	Range of values	Comments/Constraints
O/C ratio before external reformer (ζ_{oc})	2-3	Fuel dilution vs carbon deposition
External to total reforming fraction (R_{ext})	20-50%	Carbon deposition in anode vs auxiliary power consumption
Reducing species fraction at anode exhaust (ζ_{red})	10-20%	Oxidation of the Ni-YSZ anode
Air-fuel equivalent ratio in burner (λ)	1.1-4.45	System energy balance and maximum temperature in burner
Fan inlet temperature (T_{13})	200-790° C	Cold recirculation versus hot recirculation
Fan specific speed (n_s)	0.4-1.4	Fan isentropic efficiency vs. mechanical losses inside the bearings

Energy flow model

The SOFC system is composed of stack, heat exchangers (HEXs), reformer, burner, recirculation fan, and auxiliary fans. The process schematic for the co-flow stack arrangement analyzed in this work is represented in Figure 2. In this particular configuration both air and fuel enter the stack at a temperature of 680° C and exit at a temperature of 790° C. The heat fluxes Q_i can be both positive or negative depending on the optimization results.
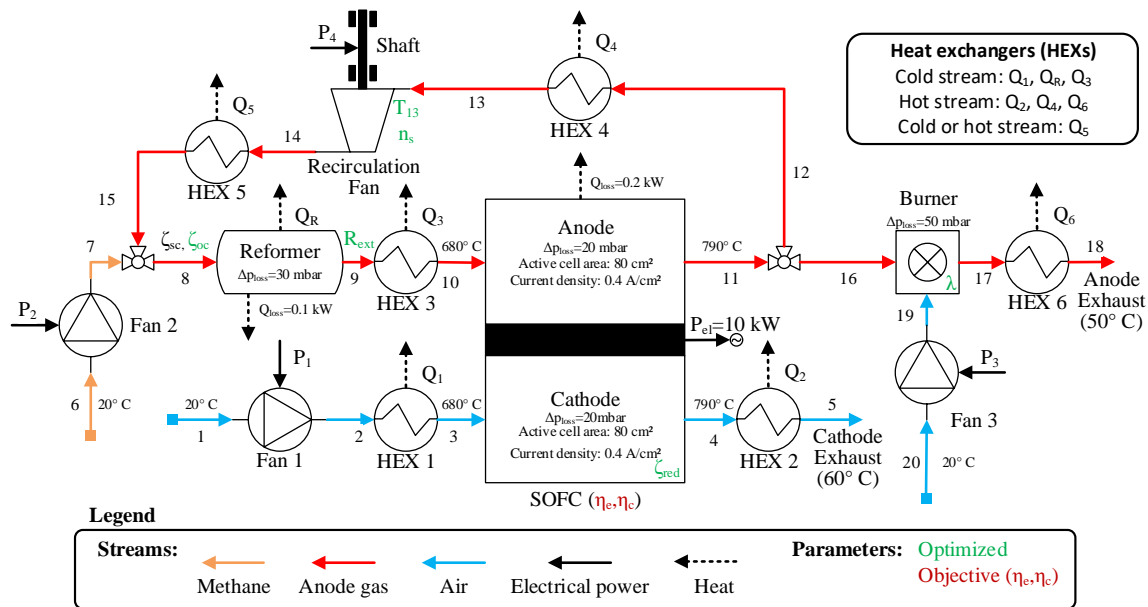
Figure 2. Process flow diagram of the considered co-flow SOFC system with 10 kW$_e$

Table II. SOFC stack parameters

Parameter	Fixed values
Pre-exponential factor cathode	4584515.9 S/cm
Anode activation energy	106000 J/mol
Cathode activation energy	101205 J/mol
Contact loss interconnect-anode	0.02 Ωcm²
Contact loss interconnect-cathode	0.03 Ωcm²
Electrolyte thickness	10 μm

Methane (6) and air (1 and 20) at a temperature of 20° C are the feed gases to the system. Their mass flows are adapted to reach the targeted 10 kW$_e$ with all SOFC system configurations. The fuel (7) mixes with the recirculated anode exhaust gas (15) and is preheated to the reformer temperature (8) determined by the external to total reforming fraction (R_{ext}) and the oxygen to carbon ratio (ζ_{oc}). Within the isothermal reformer, part of the methane is converted to hydrogen and carbon monoxide. The reforming reaction is completed within the stack (internal reforming). Oxygen from the air feed is consumed in the electrochemical reaction at the cathode. The amount of fuel utilized in the stack is determined by the reducing fuel (H_2, CO) species fraction (ζ_{red}) set at the anode exhaust. The cathode exhaust (4) is cooled down to 60° C, thus providing thermal energy (Q2 in Figure 2) to the system. A non-recirculated fraction of the anode exhaust (16) is sent to the burner, where it undergoes complete combustion with incoming fresh air, for satisfying the energy balance for the remaining endothermal processes in the system. The other anode exhaust fraction (12), determined by the oxygen to carbon (O/C) ratio before the reformer (ζ_{oc}), is recirculated. Table I describes the design variables and their range of values.

SOFC stack. In order to reduce the computational cost involved with evolutionary optimization algorithms a 0D model adapted from Van herle [11] is used here. The model parameters used in this work are summarized in Table II. The model has been validated with the performance maps of a HotBox^{TM}, the proprietary stack of HTceramix-SolidPower [12] resulting in a maximum deviation of ±1.6% for the efficiency and ±2.7% for the stack voltage within the tested boundaries between model prediction and experimental data as shown in Figure 3. Electrical DC stack LHV efficiency is reported. Both a constant stack pressure drop of 20 mbar and stack heat loss of 200 W$_{th}$ based on experimental measurements are included in the model. An additional heat loss of 100 W$_{th}$ for piping elements is also implemented.
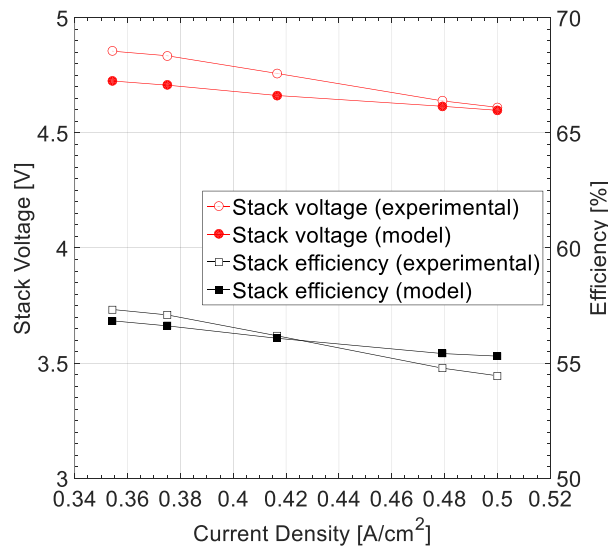

Figure 3. Comparison between experimental and simulated results for a short SOFC stack (6 cells), cell area 80 cm^2, and 75% fuel utilization

Pre-reformer. The recirculated anode exhaust (15) mixes with the incoming fuel supply (7) just upstream of the reformer. The extent of external methane reforming and water gas shift reaction, considered at equilibrium, is determined by the operating temperature in the reformer, which is part of the optimization variables. The pressure drop in the reformer is set to 30 mbar and a constant heat loss of 100 W$_{th}$ is included corresponding to experimental measurements. The equations for methane reforming and water gas shift reactions are given as follows:

$$CH_4 + H_2O \rightarrow CO + 3H_2 \tag{1}$$

$$CO + H_2O \rightarrow CO_2 + H_2 \tag{2}$$

Burner. In the burner, the unused fuel from the SOFC stack (16) mixes with fresh air (19) and undergoes complete combustion in adiabatic conditions. The heat released in the process is either used for the system energy balance or recovered for cogeneration. The steam in the burner exhaust can be condensed easily due to its higher partial pressure, leading to improved cogeneration efficiencies. A pressure drop due to thermodynamic and aerodynamic losses of 50 mbar is considered in the burner. The equations for the methane, carbon monoxide, and hydrogen combustion are given as follows:

$$CH_4 + 2O_2 \rightarrow CO_2 + 2H_2O \tag{3}$$

$$CO + 0.5O_2 \rightarrow CO_2 \tag{4}$$

$$H_2 + 0.5O_2 \rightarrow H_2O \tag{5}$$

Heat exchangers. Typical counter-flow HEXs are modeled. For system compactness and cost reductions, minimum approach temperatures in HEXs are restricted to the values summarized in Table III. Note that modeling HEX using fixed approach temperatures does not offer an optimization of the HEX size or cost.

Table III. Constraints on minimum approach temperature in HEXs

Stream	Minimum approach temperature/2 [° C]
Gas	25
Liquid/condensing	15
Reformer	50

Auxiliary fans. The air fan for the burner, as well as the cathode and anode fans are modelled with a constant efficiency of 22%. This results from an isentropic impeller efficiency of 60%, a mechanical efficiency of 40%, and an electric motor and driver efficiency of 90%. Note that Powell et al. [6] report cathode fan efficiencies of 12-15% while stating that the fans were not properly sized.

<u>Small-scale recirculation fan.</u> Since the focus of this work is on the AOR, the recirculation fan itself is modelled more in detail. Analytically derived 0D similarity concepts by Balje [13] are used to predict the fan isentropic efficiency (η) and the specific diameter (d_s) depending on the specific speed (n_s). These classical relations, however, are only valid for large scale turbomachinery, implying high Reynolds numbers in the order of 10^6. Since the recirculator for this 10 kW$_e$ system is operating at significantly lower Reynolds numbers of down to $2 \cdot 10^4$, additional aerodynamic losses will incur. The additional efficiency penalty is taken into account by the actual Reynolds number:

$$Re = \frac{\rho_1 \omega D_2 b_2}{2\mu_1} = \dot{m}_{13} \frac{\omega}{2\pi c_{m2}\mu_1} \sim \dot{m}_{13} \tag{6}$$

with the density (ρ_1) and dynamic viscosity (μ_1) at the fan inlet, fan rotational speed (ω), fan diameter (D_2), recirculated mass flow of stream 13 in Figure 2 ($\dot{m}_{13}$), trailing edge blade height (b_2), and the meridional velocity at the trailing edge (c_{m2}). A priori, the optimized AOR mass flow ($\dot{m}_{13}$), the

recirculation gas temperature (T_{13}) and composition (ξ_i) are not known. Hence, an initial optimization is needed to get a first estimate of these values. Each point on the Pareto front shown in Figure 5 corresponds to a specific system configuration with specific values of $\dot{m}_{13}$, T_{13}, and ξ_i. The mean solution values of cluster #1 and #2 for hot and cold AOR, marked with a black square in Figure 5 are used to design a nominal fan geometry that is further described in the following section.

Detailed aerodynamic fan models account for the additional losses resulting from scaling effects such as reduced Reynolds numbers and increased relative tip clearance and provide correlations for adjusted isentropic efficiencies and fan specific diameters as a function of specific speed and Reynolds number. These two functions are used for the 0D fan model within the SOFC system for the optimization as shown in Figure 1. Note that within the different system designs along the Pareto front shown in Figure 5, the recirculation mass flow rate and therefore the fan diameter vary significantly (higher mass flow implies higher fan diameters and vice versa). As a consequence, the Reynolds numbers differ by up to ±30% within the different clusters in comparison to the nominal fan geometry based on the mean value of each cluster. Since designing a new fan geometry for each iteration of the optimization process would result in a prohibitively high computational time, the values of the nominal impeller geometry have been corrected as follows [14]:

$$\eta = 1 - \left(1 - \eta_{nom}\left(n_s, \mathrm{Re}_{nom}\right)\right)\left(\frac{\dot{m}_{13,nom}}{\dot{m}_{13}}\right)^{\gamma} \qquad [7]$$

Within the four different Pareto front clusters, the velocity (c_{m2}) at the fan trailing edge and the dynamic viscosity (μ_1) vary only by ±2.5% and ±0.5%, respectively. These parameters can therefore be considered as constant along the Pareto front. As specified, for a constant specific speed, the rotational speed is kept constant and only the diameter is adjusted, hence the Reynolds number in Equation 6 is only a function of the fan inlet mass flow ($\sim\dot{m}_{13}$). The exponential factor (γ) in Equation 7 normally varies from 0.1 to 0.3 [14] and has to be specified to best fit all the different fan designs on the Pareto front as shown in the next section in Figure 14 for the case of the cold AOR.

The mechanical fan losses are modelled by assuming dynamic gas-lubricated journal and thrust bearings. In contrast to conventional ball bearings, the fan life time is increased and the shaft can run at higher rotor speeds and operational temperatures. Loss correlations as proposed by Demierre et al. [15] are used:

$$P_{radial} = \frac{1}{4}\pi D_{shaft}^3 \omega^2 \frac{\mu L}{h_{radial}} \qquad [8]$$

$$P_{axial} = \frac{1}{32}\pi\omega^2\left(D_2^4 - D_{shaft}^4\right)\frac{\mu}{h_{axial}} \qquad [9]$$

with the journal bearings length (L) and clearance (h_{radial}), the thrust bearing clearance (h_{axial}), and the shaft diameter (D_{shaft}). The bearing dimensions are directly scaled with rotor speed (Ndm number) and air at 200° C is assumed as lubricant for both the cold and the hot recirculation. This is a reasonable assumption since the recirculator will be placed within the SOFC hotbox which operates at 200°C. The design variables can be found in Table IV. Windage losses produced in the electric motor air gap are included as proposed by Mack [16]. No specific electric motor design is considered, therefore additional

losses, like iron loss in the stator and copper loss in the winding [17], are considered with a constant electric motor efficiency of 90%.

Table IV. Design parameters for the fan shaft and bearings

Variable	Value	Description
L/D_{shaft}	1	Ratio length to shaft diameter
h_{radial}/D_{shaft}	0.0007	Ratio radial clearance to shaft diameter
h_{axial}/D_{shaft}	0.0025	Ratio axial clearance to shaft diameter
Ndm number	$1.5 \cdot 10^6$ rpm·mm	Rotational speed multiplied by shaft diameter
h_{mot}	200 μm	Gap in electric motor

Heat and power integration

Besides the stack and recirculator modeling, the complete HEX network of the full system is also included into the optimization loop in order to favorize internal heat exchange over external heat input. Excess heat produced in the system is recovered for domestic heating. This cold utility undergoes heating from 20° C to 60° C. Figure 4 shows two composite curves on the Pareto Fronts in Figure 5, point A for the cold AOR and point B for the hot AOR. Cold components requiring heat input are the isothermal reformer, HEX 1 (air heater) and 3 (fuel heater). Hot sources are available in HEX 2 (stream 4, air exhaust cooling) and 6 (stream 17, fuel exhaust cooling). In the case of cold AOR, HEX 4 is a component cooling the hot recirculated anode stream 12 and HEX 5 requires reheating of this stream to the reformer inlet. In the case of hot AOR, HEX 4 is not used ($Q_4=0$) and HEX 5 requires cooling.
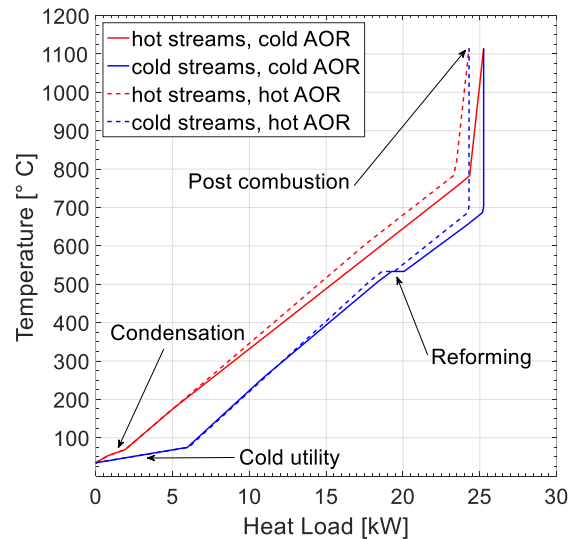

Figure 4. The SOFC system composite curve for cold AOR (solid line) and hot AOR (dashed line) at the point A, respectively B on the Pareto front shown in Figure 5.

Performance objectives and multi-objective optimization

The OSMOSE platform [18,19], a Queueing Multi-Objective Optimizer (QMOO) based on an evolutionary algorithm, is used for the system optimization. Starting with an initial population of randomly assigned design variables the flowsheet is solved for each individual set of variables. This

initial population size is chosen to 200. The individual solutions are evaluated based on the system DC net electrical efficiency:

$$\eta_e = \frac{\left(P_{el} - P_1 - P_2 - P_3 - P_4 \right)}{\dot{m}_6 \times LHV} \qquad [10]$$

and the cogeneration efficiency:

$$\eta_c = \frac{\left(P_{el} - P_1 - P_2 - P_3 - P_4 \right) + \sum Q}{\dot{m}_6 \times LHV} \qquad [11]$$

with the SOFC electrical output (P_{el}=10kW$_e$), the auxiliary equipment electrical consumption (P_1, P_2, P_3, and P_4), and the sum of heat flows ($\sum Q$) as shown in Figure 2. The Pareto front is considered to be converged, as it changes less than 0.1% from one design variable generation to the next. In this particular case this is achieved after 5'000 iterations.

System optimization results and analysis

Figure 5 shows the Pareto curves obtained from the evolutionary algorithm for a co-flow stack configuration (10 kW$_e$ electrical output) with both cold (i.e. 200° C) and hot recirculation (i.e. anode exhaust temperature). Firstly, the curves clearly identify a trade-off nature between cogeneration and electrical efficiencies. Secondly, clusters of different solutions appear for both hot and cold AOR. The formation of these clusters is a consequence of a switch between operation with lower and higher O/C ratio (see Figure 9). Further, stack operation with cold recirculation offers better performance, as the recirculation fan consumes less work with cooler fluids. DC net electrical efficiencies in excess of 64% and cogeneration efficiencies above 97% (based on the LHV) are suggested to be achievable for both hot and cold recirculation. Such high cogeneration efficiencies can be achieved, since the efficiency calculation is based on the LHV as stated in Equation 11. In addition, part of the water vapor is condensed in HEX6, as shown in Figure 2. The anode off-gas is burned with fresh incoming air at low air-fuel equivalent ratio which leads to higher partial water vapor pressure in stream 17 and thus to higher condensation and heat recovery in comparison to the case of simple anode and cathode stream mixing (4 and 11 in Figure 2). The cogeneration efficiency is not constant at 111% (HHV/LHV=1.11) for all cases on the Pareto front, because of 1.) mechanical and electrical losses in the fans, 2.) constant heat losses to the environment (in total 300 W$_{th}$), 3.) outlet streams are not cooled to the inlet temperature of 20° C, but to 50° C (anode stream) and 60° C (cathode stream), and 4.) partial condensation of the water vapor in the burner exhaust stream.
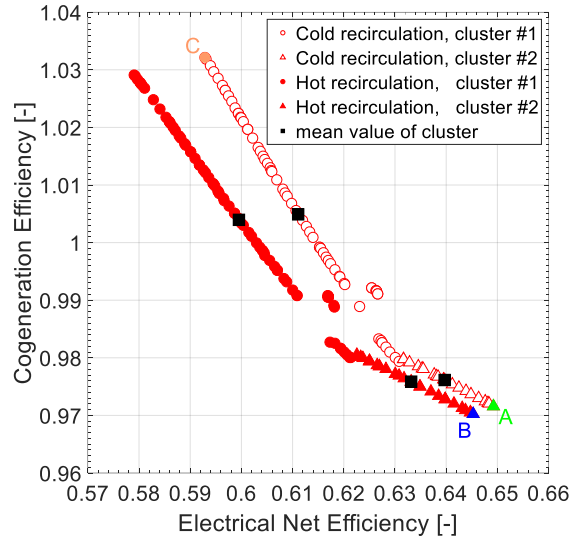
Figure 5. Pareto front of the optimized SOFC system

Highest electrical efficiency is reached at the highest fuel utilization, where cell voltage drops due to Nernst and mass transfer losses. It follows that the number of cells in the stack needs to increase to achieve the targeted electrical output power of 10 kW$_e$ given a constant current density of 0.4 A/cm² (Figure 6). Figure 7 shows the local fuel utilization, i.e. the fuel consumed between the stream 10 and 11 (Figure 2), the global fuel utilization, i.e. the fuel consumed between stream 6 and 16, and the anode off-gas recirculation fraction. A discontinuity is observed around the 62% (hot AOR), respectively 63% (cold AOR) electrical efficiency region, where the system switches from a lower local fuel utilization and higher recirculation operation (cluster #1) to a higher local fuel utilization and lower recirculation operation (cluster #2), including a drop in global fuel utilization. This accounts for the sudden voltage jump. Note that electrical efficiencies above 60% can be achieved with AOR, while keeping low local fuel utilization, which is beneficial for the SOFC stack lifetime (Figure 7).
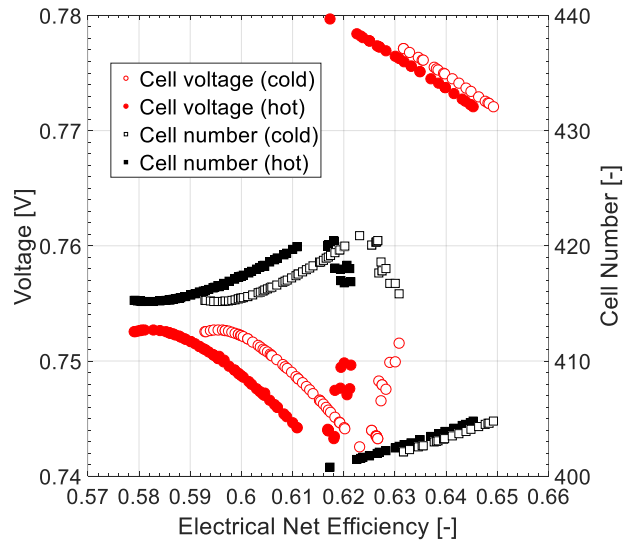

Figure 6. Evolution of the fuel cell parameters along the Pareto front (constant current density of 0.4 A/cm²)
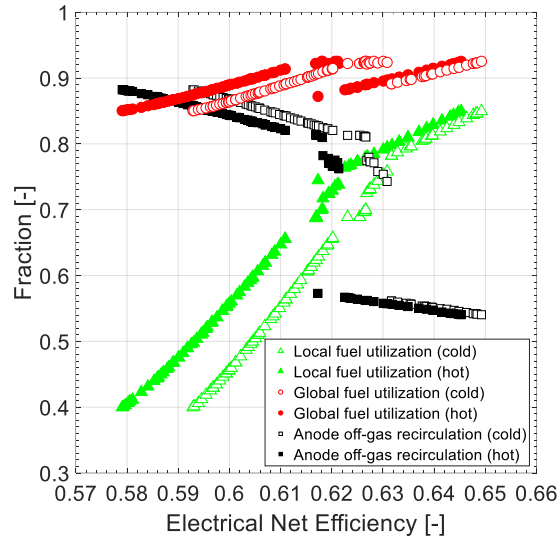
Figure 7. Evolution of anode off-gas recirculation, local and global fuel utilization along the Pareto front

At increased system net electrical efficiencies, the fuel utilization is generally high and thus a higher amount of fuel is converted. Since this is an exothermic reaction, more heat is generated in the stack. In order to limit the stack temperature gradients, the cathodic air flow increases, see Figure 8. As less fuel is available for the system energy balance, the adiabatic flame temperature in the burner decreases, with the exception around the kink corresponding to lower global fuel utilization (Figure 7). The reformer temperature tends towards lower values, in agreement with the required lower external reforming limit of 20%, based on an isothermal equilibrium model, as shown in Figure 9.
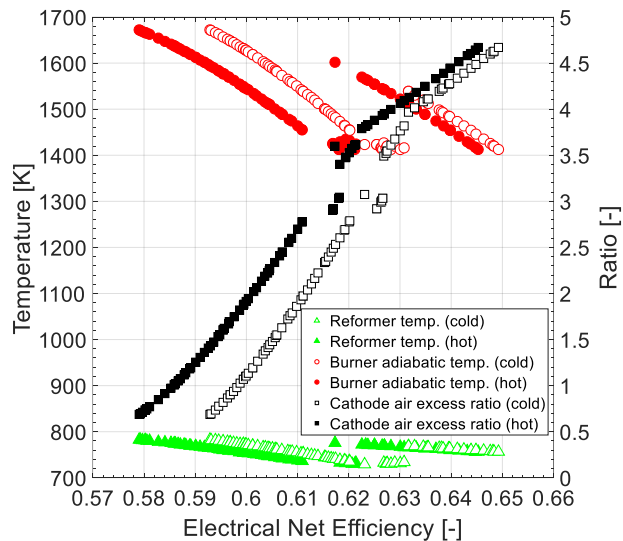

Figure 8. Evolution of system temperatures (left y-axis) and cathode air excess ratio along the Pareto front (right Y-axis)

Results in Figure 9 indicate that towards improved electrical efficiency both the fraction of reducing species (i.e. H_2 and CO) at the anode exhaust and the external reforming fraction reach their lower limits of 10% and 20%, respectively. This is a result of higher endothermic internal reforming neutralizing the

stack heat and thus reducing cathodic fan losses. An O/C ratio of 3 in the reformer corresponds to higher recirculation and lower local fuel utilization operation. As the operation mode switches, the O/C ratio in the reformer switches to the lower value of 2.
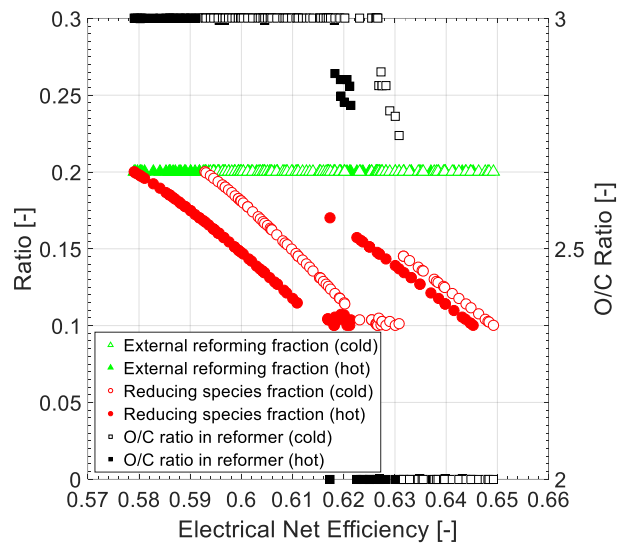

Figure 9. Evolution of three design variables along the Pareto front

In terms of fan design, the specific speed converges towards 0.98-1.05 for cold and to 0.83-0.90 for hot recirculation. According to Balje best fan efficiencies are reached at specific speeds of around 0.7 to 0.75. The optimizer therefore scarifies some isentropic fan efficiency points to obtain higher rotational speeds resulting in smaller fans and rotors, yielding lower mechanical losses and better overall performance. This clearly shows the importance of holistic approaches, when designing complex, interdisciplinary systems.

Figure 10 shows the evolution of the isentropic fan, mechanical and total efficiencies which includes an electric driving efficiency of 90% along the Pareto curves. At the best net electrical efficiency point on the Pareto front, the fan achieves an overall isentropic efficiency of 50% for cold and 43% for hot recirculation. The difference between hot and cold recirculation is due to higher dynamic viscosities and lower densities at high temperatures, resulting in lower Reynolds numbers and therefore higher viscous losses. At high cogeneration efficiencies the AOR rate is higher, thus requiring a larger fan diameter (Figure 7 and Figure 11), which leads to a slight increase in efficiency and vice versa for high net electrical efficiencies.

The electrical power input for the hot AOR is higher (from 395 to 95 W_e) compared to the cold AOR configuration (from 171 to 31 W_e). The main mechanical losses occur in the journal bearings for the cold AOR (from 18 to 7 W) and in the axial thrust bearing for the hot AOR (from 35 to 18 W). The higher values of the fan electrical power (395 W_e; 171 W_e) and mechanical losses (18 W; 15 W) refer to an SOFC system on the left side of the Figure 10, i.e. with lower net electrical efficiencies. The lower values (95 W_e; 31 W_e; 7 W; 18 W) refer to an SOFC system on the right side of the Figure 10, i.e. with higher net electrical efficiencies.

As shown in Figure 11, for higher AOR rate (towards lower net electrical system efficiency), the fan diameter is higher and the rotational speeds lower than for lower AOR rate (higher net electrical system efficiency). Rotational speeds up to 160 krpm are required for both hot and cold AOR to achieve the

pressure increase of 50 mbar. The corresponding fan diameters ranging from 20 to 30 mm are very feasible as already demonstrated in previous work by Schiffmann and Favrat [20].
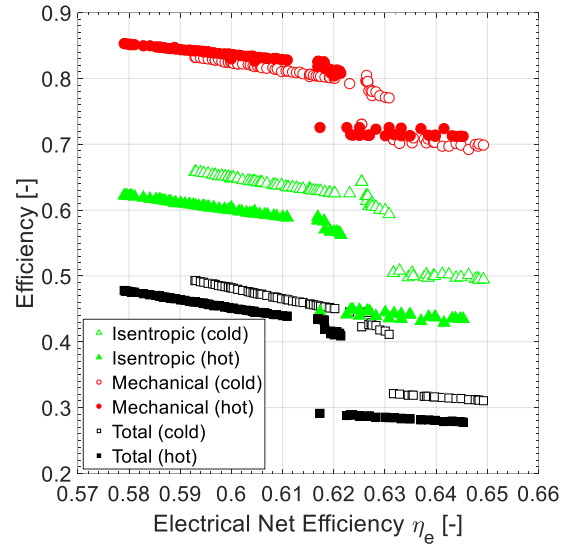

Figure 10. Evolution of isentropic fan, mechanical and total efficiencies along the Pareto front
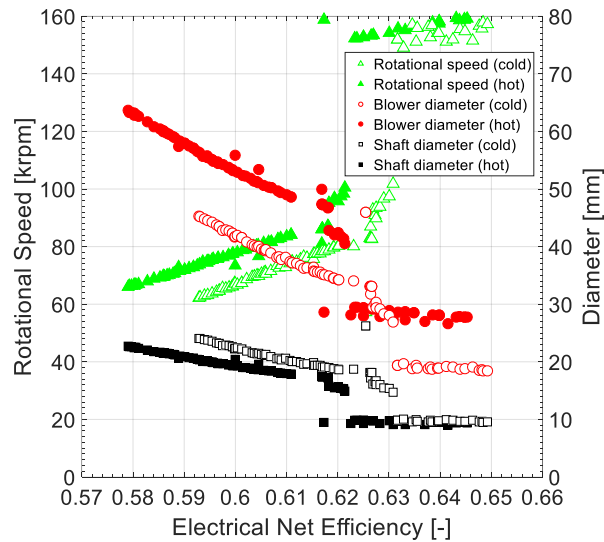
Figure 11. Evolution of rotor speeds, fan and shaft diameters along the Pareto front

The operation characteristics of the system, at the chosen point of maximum electrical efficiency, i.e. point A for hot AOR and point B for cold AOR as shown in Figure 5, are summarized in Table V. The difference in net electric efficiency is rather small although hot and cold recirculation do not represent the same system layout. Note also that the optimal recirculator design varies between the two concepts.

Table V. Operation characteristics of system at best net electrical efficiency point

	Cold AOR (point A)	Hot AOR (Point B)
SOFC stack electrical output (DC)	10 kW$_e$	10 kW$_e$
Net electrical efficiency (LHV DC)	64.9%	64.5%
Cogeneration efficiency (LHV DC)	97.2%	97.0%
No. of cells in stack	405	405
Cell voltage	0.772 V	0.772 V
Current density	0.4 A/cm²	0.4 A/cm²
Cell area	80 cm²	80 cm²
Fan specific speed	1.02	0.84
Fan speed	157.2 krpm	159.1 krpm
Fan diameter	18.4 mm	27.7 mm
Fan total efficiency	31.1%	27.7%
O/C ratio at reformer inlet	2.0	2.0
Reducing species fraction at anode exhaust	0.10	0.10
External to total reforming fraction	0.2	0.2
Fan inlet temperature	200° C	790° C
Mass flow rate methane (at 20° C)	0.291 g/s	0.291 g/s
Air excess	4.67	4.67
Single pass fuel utilization	85.0%	85.0%
Global fuel utilization	92.5%	92.5%
Anode off-gas recirculation fraction	54.1%	54.1%
Pressure drop in SOFC stack and reformer	50 mbar	50 mbar
Power consumption recirculator	38 W$_e$	95 W$_e$
Power consumption cathode fan	487 W$_e$	487 W$_e$

Detailed anode off-gas recirculation fan design and modelling

General design considerations. According to the similarity concepts based on specific speed and specific diameter proposed by Balje [13] an axial fan would result in very high rotational speeds of around 450 krpm and in exceedingly small fan diameters for point A in Figure 5. A radial configuration with lower rotational speeds is therefore preferred and more in particular a specific low-cost design for the nominal recirculation fan geometry is considered, consisting of a radial inducer-less fan with backward-curved low aspect ratio prismatic 2D blades. For such a design, the fan flow coefficient ($\phi = 8\dot{m}_{13} / \left(\pi D_2^3 \omega \rho\right)$) is typically in the lower range of 0.02 to 0.03 [21]. Impellers with low flow coefficients usually yield higher end wall friction losses within the blade channels due to a decreased hydraulic diameter and therefore achieve lower efficiencies [21–23]. In addition the high curvature at the fan inlet leads to an accelerated flow and therefore further performance losses [24]. The advantage of an inducer-less fan with two-dimensional blading is the easier manufacturing process. As a consequence shorter manufacturing time and reduced impeller production cost are expected. Additionally, blade thickness and height are kept constant to further simplify manufacturing.

The ratio of inlet hub to shroud diameter (D_{1h}/D_1) is kept at 0.5 although literature suggests lower values of around 0.3 to 0.4 [25]. Because of this high ratio, it is possible to drill eight Ø0.9 mm holes in the fan hub to facilitate the shaft balancing as shown in Figure 12.

The leading edge blade angle and height is designed to minimize the relative velocity and therefore losses as suggested by Eck [26]. As shown in Figure 15, after some acceleration induced by the axial-to-radial curvature, the flow diffuses until the trailing edge (TE). Design guidelines suggest to limit flow diffusion in the fan impeller, i.e. the ratio of relative velocities at TE and leading edge (LE) in order to avoid excessive diffusion losses [26].

Highly backward-swept blades with an angle of $\beta_2 = 75°$ are chosen to further limit the diffusion within the fan impeller. Backward-swept blades are known to improve the impeller exit flow uniformity, overall

pressure recovery and its isentropic efficiency. The main disadvantage of back-swept impellers are the higher rotational speed compared to non-swept impellers [22][27]. For the cold AOR, a total of 8 blades, half of them allocated as splitter blades, are identified as ideal number. This results from a trade-off between wall friction and slip loss at the TE.

For small-scale turbomachinery, the clearance between blade tip and shroud has a crucial influence on its performance and efficiency. In order to account for assembly, manufacturing, and bearing clearance, the fan has been designed and optimized for a tip clearance of s=80 μm.

Due to the constant blade height *b*, the meridional velocity at the impeller outlet is low. The outlet swirl parameter (c_{u2}/c_{m2}) is therefore very high (approximately 5.5). The occurrence of some backflow regions in the diffuser is therefore expected. This problem can be tackled by either pinching the diffuser or diffusing directly into the volute. The latter option is chosen to further simplify the recirculation fan geometry.
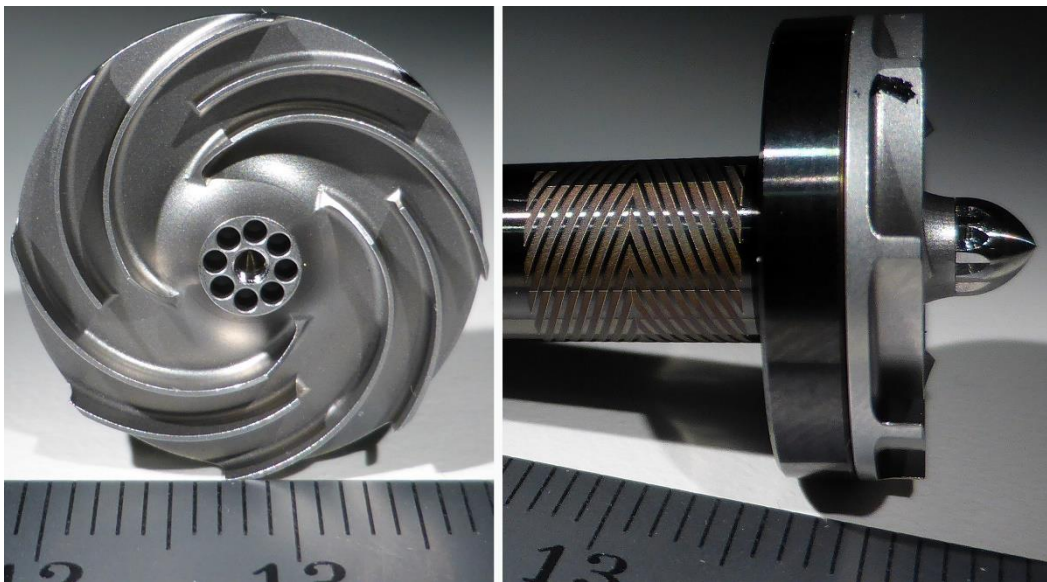

Figure 12. Anode off-gas recirculation fan design with 4 full and 4 splitter blades (left), as well as fan from the side view with mounted fan nose cone and stainless steel shaft, coated with Diamond-Like Carbide (DLC), with one of the two Herringbone Grooved Journal Bearings (right). Every tick is a one mm.

1D fan model. In comparison to standard turbomachinery, small-scale machines are subjected to several disadvantages: (1) the lower Reynolds number results in increased viscous losses, (2) manufacturing and assembly limit operation at high blade tip clearances, (3) increased relative surface roughness leads to additional friction losses, and (4) increased losses as a result of relatively thick blades.

The estimate of reduced scale turbomachinery efficiency with well-known similarity concepts is therefore challenging. For prototype turbomachines, Balje suggests to subtract 3 to 7 efficiency points from the efficiency calculated with the similarity concepts [13]. Additionally, losses occur due to the low fan flow coefficient, high relative blade thickness (t/D_2=0.01) and therefore high LE radius [13]. The incidence loss is also increased due to the two-dimensional blading. Based on aerodynamic considerations 10 points of efficiency are therefore subtracted.

The losses related to tip clearance are estimated as proposed by Pfleiderer:

$$\frac{\Delta\eta_{is}}{\eta_{is}} = a\,\frac{s}{b_2} \qquad [12]$$

with an empirical coefficient *a* ranged between 1.5 to 3 [28]. This coefficient is found to be a=2.9 for the fan geometry by comparing two CFD simulations – one with the nominal tip clearance of s=80 µm and the other with a fictitious tip clearance of s=0 µm.

The losses related to the low Reynolds numbers and the high relative surface roughness are predicted by using correlations given by Wiesner [14]. As stated in Equation 6 the Reynolds number is based on the fan outlet width b_2.

Based on a 1D mean line model, the velocity triangles, as well as static and total fluid properties at the fan inlet, leading edge (LE), TE, and diffuser outlet can be calculated (see also Figure 13). With this data and the corrected Balje isentropic efficiency, the pressure loss within the fan impeller is estimated:

$$\Delta p_{loss} = (1-\eta_{is})\bar{\rho}\Delta h \qquad [13]$$

This equation uses the mean density in the fan impeller ($\bar{\rho}$) and the specific enthalpy difference (Δh) [29]. With an iterative process, it is therefore possible to adjust the fan diameter while keeping the rotational speed constant, until the fan pressure rise converges to the desired 50 mbar. Compared to the 0D-model based on corrected specific speed and diameter correlations this iterative 1D model increases computation time by a factor of about 1000.

3D fan modelling. The estimate of the fan isentropic efficiency and pressure increase with similarity concepts and simple 1D models is limited due to the highly non-uniform flow within the impeller (formation of jet and wake – see also Figure 15). In addition, since the 1D loss correlations are validated only for large scale machines, the 1D model per se cannot be used as a reliable design tool. A CFD simulation with the commercial software ANSYS CFX is therefore used to verify the fan parameters and design the fan blade shape.

The 1D geometric data is used to construct a 3D geometric model with ANSYS BladeGen. As shown in Figure 13, the geometric model consists of an inlet duct (the fan nose cone is neglected), the fan impeller, and a diffuser (not shown in Figure 13). Only one passage including the main and splitter blade is modelled. The fan blade shape is controlled by the blade angles at the hub profile. The spanwise distribution type is set to "axial element" to obtain prismatic blades. The blade angle with respect to the meridional surface at the TE (β_2) is maintained at 75°. LE and TE both have an elliptic ratio of 2.0, respectively 1.0 as grid generation is less complex. In Figure 12 the LE is manufactured as square and the TE as cut-off which will be changed later to elliptical. As already mentioned, the blade thickness is constant in the span-wise (hub-to-shroud) and streamwise direction (LE to TE). The hub fillets caused by the manufacturing (0.4 mm) are not included in the simulation. The splitter blades begin from a meridional distance of approximately 55% from LE and follow the blade angle and thickness distribution of the main blades.

The "ATM Optimized" topology in ANSYS TurboGrid is used to create a 3D structured grid based on hexahedral elements. The main blade near-wall y^+ values are maintained from 0.1 to 6 to resolve the viscous sublayer in the boundary layer. The average y^+ value is below 2 – only in the area of the LE the high y+ values of up to 6 are reached. The tip-clearance gap of 80 µm between the fan shroud and blades is introduced by trimming down the fan blades. Table IV contains the results of a grid independence study. The grid is refined from 0.4, to 0.6, 1.2, 2.8, 5.1, and 9.2 million elements. The fan impeller is

simulated at nominal operation and its total to total pressure rise and the isentropic efficiency are compared. The difference between two consecutive values is below 1% for a grid size higher than half a million elements, which is therefore considered to be a suitable choice.

Table VI. Grid independence study for best net electrical efficiency and cold AOR (fan with 5+5 blades)

Number of elements in million [-]	0.37	0.61	1.2	2.8	5.11	9.16
Total to total pressure difference Δp [mbar]	73.79	73.01	73.06	72.96	73.08	73.03
Difference between two consecutive values [%]		-1.1	+0.1	-0.1	+0.2	-0.1
Isentropic efficiency η_{is} [%]	49.96	49.85	49.85	50.00	50.49	50.32
Difference between two consecutive values [%]		-0.2	0	+0.3	+1.0	-0.3

In order to limit computational time, only a single passage, i.e. ¼ of the fan impeller section shown in Figure 13, is simulated. At the inlet, the AOR gas composition, total temperature and pressure are specified. At the outlet, the mass flow is imposed. All the wetted surfaces have been considered as hydraulically smooth; hence surface roughness is not defined and skin friction loss is only caused by fluid viscosity. A compressible, non-isothermal, homogeneous multiphase fluid, consisting of water vapor, hydrogen, carbon dioxide and monoxide, is chosen. The k-ω shear stress transport turbulence model with a moderate turbulence intensity of 5% at the fan inlet boundary is specified.
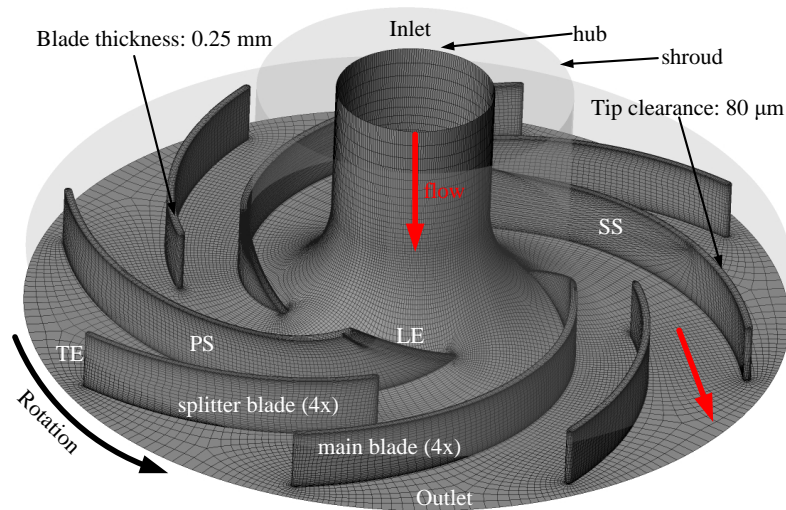

Figure 13. Illustration of the full computational recirculator domain and grid

Blade design. Due to the difference in pressure on the blade Suction Side (SS) and Pressure Side (PS), as shown in Figure 13, a tip leakage flow is developed, which creates a vortex structure that stretches stream-wise in the blade passage causing considerable performance loss. In order to delay this vortex generating mechanism and therefore reduce the impact of large relative tip clearance, Adeel et al. recommend aft-loaded blades for small-scale turbomachinery operated at high relative tip clearance [25]. Hence, the first 22% (based on meridional coordinate) of the main blades after the LE are designed with a low loading, i.e. the blades only transfer little mechanical work to the fluid. The last 78% of the blades towards the TE have logarithmic shape, i.e. with constant blade angle, leading to an increased blade loading towards the TE.

Modeling comparisons and results. Table VI contains fan parameters for a specific speed of n_s=1.02, a total to static pressure increase of 50 mbar, and cold anode off-gas recirculation at 200° C for the SOFC system configuration with (1) the best net electrical efficiency (marked A on the Pareto front in Figure 5) and (2) the best cogeneration efficiency (marked B on the Pareto front). According to the unmodified Balje similarity concepts, a fan efficiency of around 86% can be reached. With the efficiency drops estimated with the 1D code, the efficiency is decreased by 36.4% points (to 49.7%), respectively 20.3% points (to 65.8%). The diameter is therefore increased by 3.4 mm and 5 mm respectively in order to obtain the same pressure increase at a rotational speed of 157 krpm, respectively 62 krpm. According to the CFD results, the simulated impeller with a diameter of 19.2 mm, rotating at the same speed results in a pressure increase of 45 mbar for the 4+4 blade fan and 47 mbar for the 5+5 blade fan. The isentropic total to static efficiency:

$$\eta_{is} = \frac{\overline{h}_{t,1} - \overline{h}_{is,st,2}}{\overline{h}_{t,1} - \overline{h}_{t,2}} \qquad [14]$$

is within the same range. The adjusted similarity concepts based 0D model used within the SOFC system optimization predicts the impeller diameter 0.8 mm, respectively 0.4 mm too small, suggesting a sufficiently good agreement for the integrated optimization. The fan efficiency for the best SOFC cogeneration efficiency is underestimated by 5% points and the pressure increase is 7 mbar lower than predicted by the more simple 0D and 1D models. The fan rotational speed and/or diameter needs therefore adjustment, what leads to higher mechanical losses in the bearings.

Figure 14 compares the prediction of the 0D model that was used for the integrated optimization with the 1D-model for the design refinement, as well as with two 3D CFD calculations. The 0D model is Reynolds number corrected according to Equation 7. The nominal 0D models are based on the solutions of the two mean values of cluster #1, and #2 respectively for the cold AOR (shown as black squares in Figure 5). They show good agreement with the 1D model and 3D CFD, in particular for the solutions around cluster #2, where the relative difference is less than 1%. For the solutions around cluster #1 the maximum difference between 0D and 1D model is below 3%. This justifies the use of a simplified 0D-model for the integrated system optimization.

Table VI. Fan parameters for hot and cold recirculation predicted with different methods

| Method	Balje	0D	1D	3D	
(1) Cold AOR, best net electrical efficiency (point A on Pareto front)					
Number of blades	-	-	-	5+5	4+4
D [mm] - variable	15.8	18.4	19.2	19.2	
N_{rot} [krpm] - fixed	157	157	157	157	
$\Delta p_{t,st}$ [mbar]	50	50	50	47	45
η_{is} [%]	86.1	49.4	49.7	49.9	50.0
(2) Cold AOR, best cogeneration efficiency (point C on Pareto front)					
Number of blades	-	-	-	5+5	6+6
D [mm] - variable	40.7	45.3	45.7	45.7	
N_{rot} [krpm] - fixed	62	62	62	62	
$\Delta p_{t,st}$ [mbar]	50	50	50	43	38
η_{is} [%]	86.1	65.8	65.8	70.8	64.1
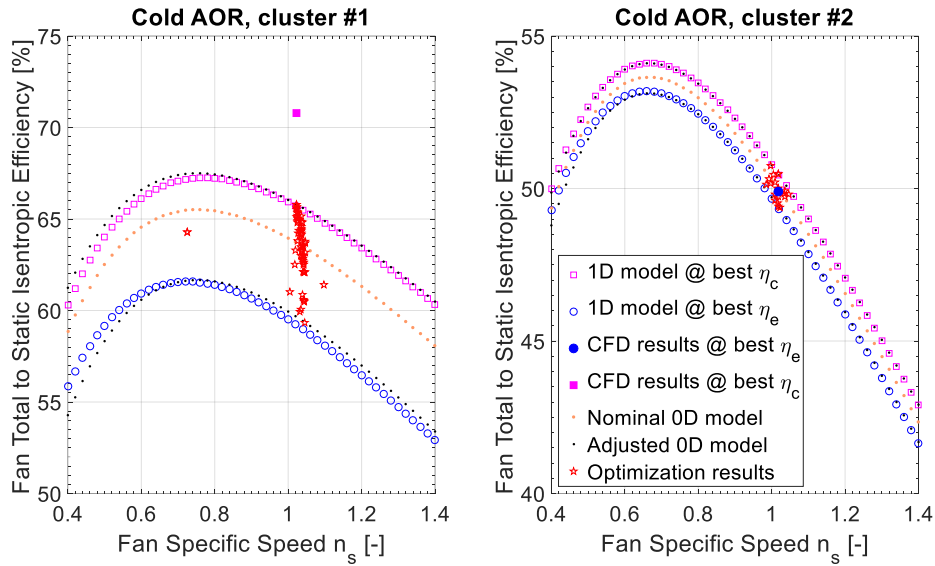
Figure 14. Fan efficiencies for the SOFC system with cold AOR, calculated with the 0D (similarity concepts), 1D, and 3D model for different specific speed values. Optimized specific speed values are indicated with red stars.

Figure 15 represents the mass flow averaged relative velocity in the meridional view of the fan impeller operated at point A on the Pareto front. Due to the high axial to radial curvature at the shroud inlet, a flow recirculation zone is formed directly after the fan LE represented by the dashed line. The effective flow passage area is therefore reduced and the flow is accelerated to 110 m/s shortly after the splitter blade LE. Towards the TE the flow decelerates to an average velocity of 86 m/s. An additional effect on the flow field can be seen as a result of tip clearance (80 μm for a blade height of 1.9 mm). A tip clearance leakage flow from the pressure side of the main blade forms that hits the LE of the splitter blade with a high incidence angle (~90°) inducing recirculation flows in the blade channel between the splitter blade suction side and the main blade pressure side within span regions above 85%, marked with a black dotted line in Figure 15.
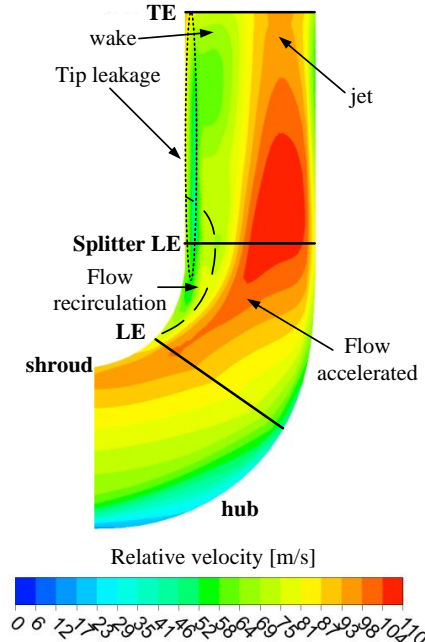

Figure 15. Meridional view of fan impeller with relative velocity flow field

Rotordynamic integrity of the fan rotor

Self-acting gas-lubricated bearings of herringbone groove type [30] have been selected to support this high-speed fan (see Figure 12 on the right). This is a compromise resulting of rotor speed, as well as temperature and lifetime expectation. Since rotor supported on gas-lubricated bearings tend to be unstable it needs to be made sure that the fan shaft can be operated stable within the entire operation range. The approach used here is similar to the validated one as implemented by Schiffmann [20,31,32]. Since the shaft is operated well below the first bending frequency, a one-dimensional rigid-body model is used. It has five degrees of freedom including axial and radial displacements, as well as two tilting motions around the center of gravity. The resulting second order differential equation is an eigenvalue problem. The ratio of the real part of these eigenvalues (λ_j) to the imaginary part (ω_j), the logarithmic decrement:

$$\Gamma_j = -\lambda_j \frac{2\pi}{\omega_j} \quad [15]$$

is commonly used as criteria for the rotor stability: if this number is higher than zero ($\Gamma > 0$) over the complete operating range, the rotor is stable.

Besides the system mass inertia matrix, also the bearing damping and stiffness matrices are used to formulate the rotor differential equation of motion. The laminar flow phenomena within the journal and axial bearings are governed by the Reynolds equation [33]. Using the narrow groove theory, a modified Reynolds equation is obtained that is linearized by applying the perturbation method. This allows to calculate the aerodynamic fluid film bearings' properties that not only depend on the rotor rotational speed, but also on the excitation frequency.

Figure 16 shows the whirl speed map of the recirculator rotor of point A on the Pareto front for the conical and cylindrical modes with the corresponding logarithmic decrements. The green circles correspond to the forward whirl due to unbalance forces whereas the red circles correspond to the backward whirl due to friction forces. During the ramp up to the nominal speed, one cylindrical mode at around 142 krpm is passed. As the rotor is sufficiently damped in this region ($\Gamma > 0.25$) no rotordynamic instabilities are expected. The first flexural mode (not shown in Figure 16) is estimated at around 900 krpm. Concerning the nominal operational speed of 157 krpm, the safety margin is therefore very high.
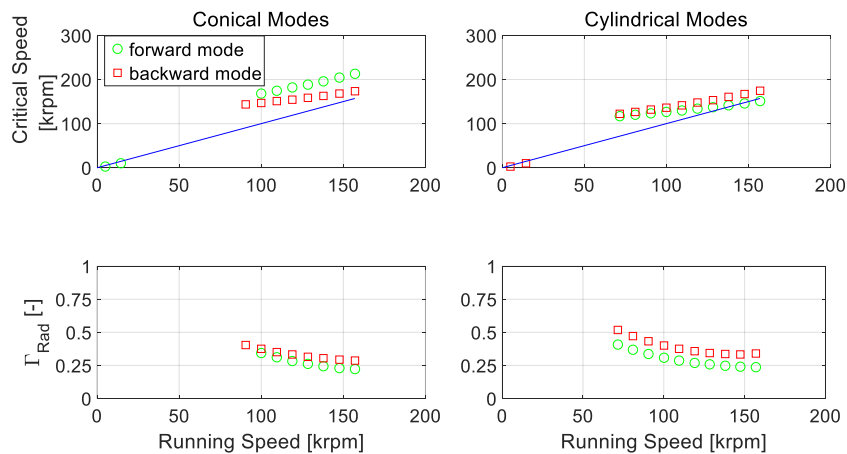

Figure 16. Campbell diagram of the rotor with forward (green circle) and backward (red square) modes and corresponding logarithmic decrements

Conclusion

Evolutionary algorithms can aid in the optimization of SOFC systems. Co-flow stack operation with cold recirculation seems to be the best operation strategy. Hot recirculation at high net electrical efficiency is also promising. This could possibly save some investment cost by avoiding additional HEX (4 and 5 in Figure 2) needed for cooling and heating of the AOR. A clearer picture could be obtained with the implementation of a third objective for the multi-objective optimization, the system cost. This would help for cost minimization and towards a more market-oriented SOFC system design. Additionally, realistic pressure drops within pipes and HEXs could give a better estimate of auxiliary costs what also effects the final system cost. It is shown that electrical efficiencies well in excess of 60% (based on the LHV) can be achieved.

The extension of the system multi-objective optimization with an observation-based fan design and simulation methodology helps to verify the results. For the case of the small-scale prismatic recirculation fan, it was found that conventional similarity concepts overestimate the efficiency by more than 36% points. A simple one-dimensional methodology is proposed to find more realistic fan efficiencies.

Acknowledgement

References

[1]   Zhao, Y., Xia, C., Jia, L., Wang, Z., Li, H., Yu, J., and Li, Y., 2013, "Recent Progress on Solid Oxide Fuel Cell: Lowering Temperature and Utilizing Non-Hydrogen Fuels," Int. J. Hydrog. Energy, **38**(36), pp. 16498–16517.

[2]   Facchinetti, E., 2012, "Integrated Solid Oxide Fuel Cell - Gas Turbine Hybris Systems with or without CO2 Separation," PhD, EPFL.

[3]   Payne, R. J., Love, J., and Kah, M., 2011, "CFCL's BlueGen Product," ECS Trans., **35**(1), pp. 81–85.

[4]   Autissier, N., 2008, "Small Scale SOFC Systems: Design, Optimization and Experimental Results," EPFL.

[5]   Peters, R., Deja, R., Blum, L., Pennanen, J., Kiviaho, J., and Hakala, T., 2013, "Analysis of Solid Oxide Fuel Cell System Concepts with Anode Recycling," Int. J. Hydrog. Energy, **38**(16), pp. 6809–6820.

[6]   Powell, M., Meinhardt, K., Sprenkle, V., Chick, L., and McVay, G., 2012, "Demonstration of a Highly Efficient Solid Oxide Fuel Cell Power System Using Adiabatic Steam Reforming and Anode Gas Recirculation," J. Power Sources, **205**, pp. 377–384.

[7]   Halinen, M., Rautanen, M., Saarinen, J., Pennanen, J., Pohjoranta, A., Kiviaho, J., Pastula, M., Nuttall, B., Rankin, C., and Borglum, B., 2011, "Performance of a 10 kW SOFC Demonstration Unit," ECS Trans., **35**(1), pp. 113–120.

[8]   Halinen, M., Pohjoranta, A., Kujanpää, L., Väisänen, V., and Salminen, P., 2014, *Summary of the RealDemo – Project 2012-2014*, VTT Technical Research Centre of Finland.

Patrick H. Wagner   21   JEECS-16-1126

[9] Palazzi, F., Autissier, N., Marechal, F. M. A., and Favrat, D., 2007, "A Methodology for Thermo-Economic Modeling and Optimization of Solid Oxide Fuel Cell Systems," Appl. Therm. Eng., **27**(16), pp. 2703–2712.

[10] Facchinetti, E., Favrat, D., and Marechal, F., 2014, "Design and Optimization of an Innovative Solid Oxide Fuel Cell–Gas Turbine Hybrid Cycle for Small Scale Distributed Generation," Fuel Cells, **14**(4), pp. 595–606.

[11] Van herle, J., Maréchal, F., Leuenberger, S., and Favrat, D., 2003, "Energy Balance Model of a SOFC Cogenerator Operated with Biogas," J. Power Sources, **118**(1–2), pp. 375–383.

[12] Modena, S., Ceschini, S., Contino, A. R., Bini, R., Tognana, L., Bertoldi, M., and Wuillemin, Z., 2013, "Evolution of SOFCpower' Stack Performances," ECS Trans., **57**(1), pp. 359–366.

[13] Balje, O. E., 1981, *Turbomachines : A Guide to Design, Selection and Theory*, New York a.o. : Wiley.

[14] Wiesner, F. J., 1979, "A New Appraisal of Reynolds Number Effects on Centrifugal Compressor Performance," ASME Trans. J. Eng. Power, **101**, pp. 384–392.

[15] Demierre, J., Rubino, A., and Schiffmann, J., 2014, "Modeling and Experimental Investigation of an Oil-Free Microcompressor-Turbine Unit for an Organic Rankine Cycle Driven Heat Pump," J. Eng. Gas Turbines Power, **137**(3), pp. 032602–032602.

[16] Mack, M., 1967, "Luftreibungsverluste bei elektrischen Maschinen kleiner Baugröße," T. H., F. f. Maschinenw.

[17] Zwyssig, C., Round, S. D., and Kolar, J. W., 2006, "Analytical and Experimental Investigation of a Low Torque, Ultra-High Speed Drive System," *Conference Record of the 2006 IEEE Industry Applications Conference, 2006. 41st IAS Annual Meeting*, pp. 1507–1513.

[18] Leyland, G., 2002, "Multi-Objective Optimisation Applied to Industrial Energy Problems," EPFL.

[19] Molyneaux, A., 2002, "A Practical Evolutionary Method for the Multi-Objective Optimisation of Complex Integrated Energy Systems Including Vehicle Drivetrains," EPFL.

[20] Schiffmann, J., and Favrat, D., 2010, "Design, Experimental Investigation and Multi-Objective Optimization of a Small-Scale Radial Compressor for Heat Pump Applications," Energy, **35**(1), pp. 436–450.

[21] Ronald H. Aungier, 2000, *Centrifugal Compressors: A Strategy for Aerodynamic Design and Analysis*, ASME Press, New York.

[22] N. A. Cumpsty, 2004, *Compressor Aerodynamics*, Krieger Publishing, Malabar, Florida.

[23] Klaus H. Lüdtke, 2004, *Process Centrifugal Compressors: Basics, Functions, Operation, Design, Application*, Springer, Berlin.

[24] Rusch, D., and Casey, M., 2013, "The Design Space Boundaries for High Flow Capacity Centrifugal Compressors," J. Turbomach., **135**(3), pp. 543–556.

[25] Javed, A., Arpagaus, C., Bertsch, S., and Schiffmann, J., 2016, "Small-Scale Turbocompressors for Wide-Range Operation with Large Tip-Clearances for a Two-Stage Heat Pump Concept," Int. J. Refrig., **69**, pp. 285–302.

[26] Bruno Eck, 2003, *Ventilatoren : Entwurf und Betrieb der Radial-, Axial- und Querstromventilatoren*, Springer, Berlin.

[27] Japiske, D., 1996, *Centrifugal Compressor Design and Performance*, Concepts ETI, Wilder, VT.

[28] Pfleiderer, C., 1961, *Die Kreiselpumpen für Flüssigkeiten und Gase: Wasserpumpen, Ventilatoren, Turbogebläse, Turbokompressoren*, Springer-Verlag, Berlin etc.

[29] R. I. Lewis, 1996, *Turbomachinery Performance Analysis*, Arnold, London.

[30] Demierre, J., Favrat, D., Schiffmann, J., and Wegele, J., 2014, "Experimental Investigation of a Thermally Driven Heat Pump Based on a Double Organic Rankine Cycle and an Oil-Free Compressor-Turbine Unit," Int. J. Refrig., **44**, pp. 91–100.

[31] Schiffmann, J., 2015, "Integrated Design and Multi-Objective Optimization of a Single Stage Heat-Pump Turbocompressor," J. Turbomach., **137**(7), pp. 071002–071002.

[32] Schiffmann, J., and Favrat, D., 2010, "Integrated Design and Optimization of Gas Bearing Supported Rotors," J. Mech. Des., **132**(5), pp. 051007–051007.
[33] W. A. Gross, 1962, *Gas Film Lubrication*, Wiley, New York etc.

Nomeclature

A = area, m^2
a = empirical coefficient, -
AOR = Anode Off-gas Recirculation
b = blade height, m
c = absolute velocity, m/s
CFD = Computational Fluid Dynamics
D = diameter, m
DC = Direct Current
d_s = specific diameter, -
h = bearing or shaft clearance, m
$\bar{h}$ = mass flow averaged specific enthalpy, J/kg
HEX = Heat EXchanger
HHV = Higher Heating Value
L = length, m
LE = Leading Edge
LHV = Lower Heating Value
ṁ = mass flow rate, kg/s
MOO = Multi-Objective Optimization
n_s = specific speed, -
O/C = Oxygen to Carbon
p = pressure, Pa
P = power, Watt
PS = Pressure Side
Q = heat flow, W
r = radius, m
Re = Reynolds number, -
R_{ext} = external to total reforming fraction, -
s = blade tip clearance, m
SOFC = Solid Oxide Fuel Cell
SS = Suction Side
T = temperature, K
t = blade thickness, m
TE = Trailing Edge
w = relative velocity, m/s
β = blade angle, measured with respect to the meridional surface, rad
Γ = logarithmic decrement, -
γ = exponential factor, -
Δh = enthalpy difference, J/kg
ζ_{oc} = O/C ratio in external reformer, -
ζ_{red} = Reducing species fraction at anode exhaust, -
η = efficiency, -
θ = azimuth angle, rad
λ = air-fuel equivalent ration in burner, -

λ_j = real part of eigenvalues, -
μ = dynamic viscosity, Pas
ξ = mass fraction, -
ρ = density, kg/m^3
ϕ = flow coefficient, -
ω = rotational speed, 1/s
ω_j = imaginary part of eigenvalues, -

Subscripts
1 = inlet
2 = fan trailing edge
el = electrical
h = hub
is = isentropic
m = meridional
nom = nominal
st = static
t = total
u = circumferential